Article

Large deformation finite element analyses for 3D X-ray CT scanned microscopic structures of polyurethane foams

Makoto Iizuka [1,*], Ryohei Goto [2], Petros Siegkas [1], Benjamin Simpson [1] and Neil Mansfield [1]

[1] Department of Engineering, School of Science and Technology, Nottingham Trent University, Clifton Lane, Nottingham NG11 8NS, United Kingdom
[2] Bridgestone Corporation, 1, Kashio-Cho, Totsuka-Ku, Yokohama, Kanagawa 244-8510, Japan
* Correspondence: makoto.iizuka@ntu.ac.uk

Version February 12, 2021 submitted to Journal Not Specified

Abstract: Polyurethane foams have unique properties that make them suitable for a wide range of applications, including cushioning and seat pads. The foam mechanical properties largely depend on both the parent material and the foam cell microstructure. Uniaxial loading experiments, X-ray tomography and finite element analysis can be used to investigate the relationship between the macroscopic mechanical properties and microscopic foam structure. Polyurethane foam specimens were scanned using X-ray computed tomography. The scanned geometries were converted to 3D CAD models using open source, and commercially available CAD software tools. The models were meshed and used to simulate compression tests using the implicit finite element method. The calculated uniaxial compression tests were in good agreement with experimental results for strains up to 30%. The presented method would be effective in investigating the effect of polymer foam geometrical features in macroscopic mechanical properties, and guide manufacturing methods for specific applications.

Keywords: Polyurethane foam; Structure–property relationships; Finite element analysis; Microscale analysis; X-ray computed tomography

1. Introduction

Polyurethane foams have many unique properties such as elasticity, softness and ease of forming. These properties make polyurethane foams attractive to automotive seat designers since they can effectively support the human body and distribute the body pressure. The improvement of the mechanical properties of the foams is an important challenge. Controlling the mechanical properties of foams would be useful for designing seats that are more comfortable and potentially at lower cost. The mechanical properties of polyurethane foams largely depend on their microstructures (Figure 1). The foam structure consists of a cluster of bubbles and struts at the edges of the cells. Figure 1 shows an example of an open-cell foam in which the bubbles are linked together. The macroscopic stress-strain relationship depends on the mechanical properties of the parent material, of which the struts are made, and the geometrical structure of cells and struts [1]. Understanding the relationships between the microscopic geometrical structures and the macroscopic mechanical properties is essential for developing foam products with superior mechanical properties.

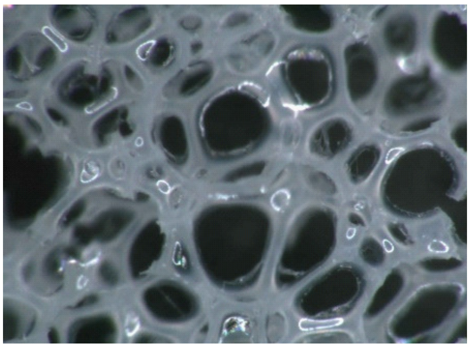

Figure 1. An example of optical microscope images of polyurethane foams

Three main regions can be identified in the stress-strain curve for the compressive deformation of elastomeric foams [1]. The typical stress-strain curve under the uniaxial compression of foams is shown in Figure 2. Linear elasticity is shown in the small strain region followed by a collapse plateau, and then densification appears accompanied by a rapid increase in the stress. Firstly, the struts bend and the macroscopically linear elastic behaviour is shown. Next, due to the increase of the macroscopic stress, some struts start buckling and the slope of the curve decreases. Finally, the slope of the curve increases again up to the same value as the matrix material, because of the contact between struts. The contribution of microstructures to macroscopic properties depends on these deformation mechanisms.

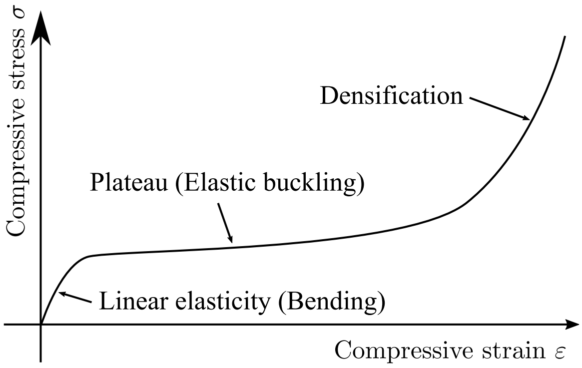

Figure 2. The typical stress-strain relationship of elastomeric foams under the uniaxial compressive stress

To investigate the effect of microstructures on macroscopic properties, cell structure geometries are virtually generated, and their deformations are analysed [2]. The cells were postulated to have same size and the shape of the Kelvin tetrakaidecahedron. The edges of the polyhedron were assumed to be struts represented by Euler-Bernoulli beams and the macroscopic elastic properties were analytically calculated. This approach was also expanded to the large compressive strain range up to 70% [3,4] and creep deformations [5]. Other researchers repeated the calculations of Zhu et al. [2], employing a finite element approach, while still making use of Kelvin's cell shape and Euler-Bernoulli beams [6–10]. As the Kelvin's cell has anisotropic mechanical properties, Okumura et al. [11] and Takahashi et al. [12] analysed the mechanical responses in the [001], [011] and [111] directions. Furthermore, closed cell foams have been analysed with shell elements [13]. Modelling the microscopic structures of polyurethane foam materials using the Kelvin's cell is thought to be a simple and effective way to investigate the deformation behaviour.

The Kelvin cell approach assumes that the microstructure is homogeneous; however, in contrast cell structures are generally heterogeneous. This is a significant disadvantage of the repeated unit cell modelling approach [14]. To model the inhomogeneous structures of foams, the 2D and 3D Voronoi tessellations were employed and the Voronoi edges were regarded as struts [14–17]. Moreover, faces in Voronoi polyhedrons were assumed as cell membranes in closed cell foams [18,19]. The elastic properties in the small strain region and the compressive stress-strain curves on the plateau region were calculated by the finite element method using beam elements. Furthermore, although the cross-sectional area of a strut is often assumed constant, the central parts of struts are thinner than other parts. The effect of this necking can be taken into account by using solid elements [11,12,20–27] or beam elements with variable cross-sectional properties [23,28–33]. In addition, the curvature of struts were modelled [34]. Models that consider the heterogeneity of foams are thought to show better results than Kelvin cell models with straight struts. Dynamic crushing behaviour [35,36] and multiaxial crushing [37] were also analysed.

One effective method to obtain a more adequate model that represents actual foam microstructures, is to use X-ray computed tomography (CT). The X-ray CT has been performed in order to observe the microstructures of various kinds of porous materials, for example, biomaterial scaffolds [38,39], soil materials [40] and polyurethane foams [41]. Therefore, the X-ray CT has also been used to generate the geometries for finite element analyses. For example, finite element models for the microstructure of a trabecular bone was generated based on micro-CT[42]. For artificial foam materials, Jeon et al. [43] analysed closed-cell aluminium foams with finite element models meshed with solid tetrahedron elements. The compressive stress-strain curves of the foam were calculated and compared to experimental results and the 20.86% volume error was shown up to 5.31% strain. Similarly, linear elastic properties under the small strain regions were obtained from X-ray CT scanned finite element models for ceramic foams [44] and a rigid organic foam [45]. Models obtained from the X-ray CT have been effectively used to investigate the mechanical properties of foams under small deformations.

For cushioning products such as automotive seat pads or bed mattresses, the mechanical properties in the plateau regions are more important than the linear elastic regions. As the slope of the stress-strain curve decreases in the plateau region, elastic foams soften and help to distribute body pressure. Most studies employ tetrahedron meshing due to the complexity of the geometry, however, this makes analysing large deformations difficult. To analyse the deformation within the plateau region, hexahedron meshing is required as it is more suitable for large deformation problems.

This study aims to use X-ray CT scans of foam specimens in order to construct validated finite element (FE) models that can be used to study and manipulate the foam microstructure for achieving desirable stress-strain behaviour in the plateau region. The microstructures of elastic polyurethane foams for automotive seat pads are scanned using X-ray computed tomography and converted to STL files. The STL files are smoothed and converted to solid CAD files with commercial CAD software so that they can be meshed with a hexahedron dominant solid mesh. The uniaxial compressive deformation of the models are analysed with a finite element method and compared with the experimental results.

2. Materials and Methods

The methodology to analyse the deformation of X-ray CT scanned foam materials and the materials supplied to validate its accuracy are explained here. The specimens were scanned using X-ray CT, converted to CAD models and analysed with the implicit finite element method. The tools used for this study is either commercially available CAD or open-source software. Moulded elastic polyurethane foams were investigated using the presented method and physically tested to compare with the result of the analyses.

2.1. Materials

The tested materials were supplied by Bridgestone Corporation. Polyols, isocyanates, water and low amounts of other materials were mixed and poured into a $400 \times 400 \times 100(\mathrm{mm}^3)$ sized mould and then expanded and polymerized. After demoulding, the foams were crushed between rollers so that cell membranes were broken and resulted in open-cell foams. The foams were left at least 24 hours before proceeding to any other process of the investigation to let the chemical reactions be completed.

The foam materials investigated in this study are mainly used for automotive seat pads by moulding in product shaped moulds.

2.2. Scanning by the X-ray computed tomography

Specimens from the centre of larger samples were cut into $5 \times 5 \times 5(\mathrm{mm}^3)$ sized cubes. The X-ray tomography equipment employed for this study was the ScanXmate RA150S145/2Be, a product of Comscantecno Co.,Ltd. Figure 3, shows an example X-ray CT scan image of the foam. The white parts indicate the foam struts and the black parts are the pores. The size of the pixel was 7.5(μm). The cross section images were taken by rotating the specimens every 0.18deg so that the cell structures could be observed in three dimensions.

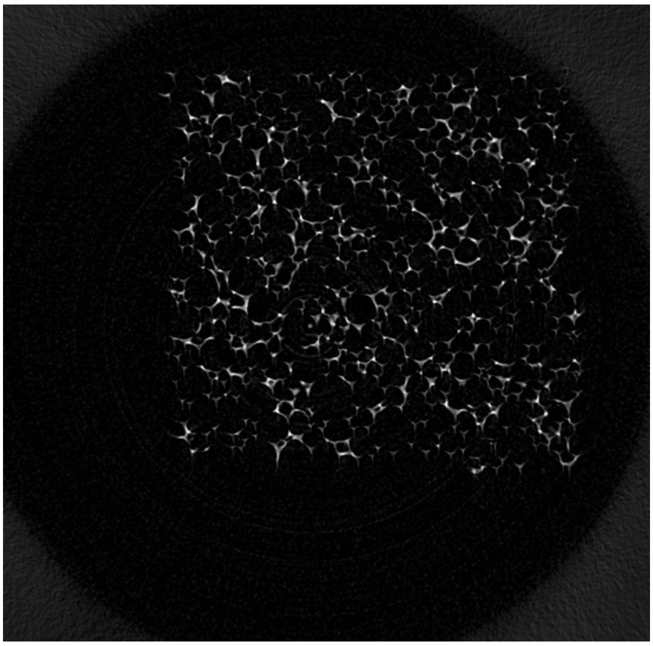

Figure 3. An example of the X-ray CT scanned images for the polyurethane foams

2.3. Converting the scanned images to 3D STL files

The cross sectional 2D images were converted to 3D STL files by Fiji [46], a distribution of Image J2 [47]. Firstly, the scanned images were binarized to black and white images using a threshold of the brightness. The threshold was determined using Otsu's method [48] and verified by comparing the relative densities measured with the actual specimen and calculated from the computational models. The borders between the black and white pixels were regarded as the surfaces of the struts. Triangles were then applied to the strut surfaces and the resulting surfaces exported as STL files. An example STL file is shown in Figure 4(a).

2.4. Converting to smoothed solid CAD models

The STL formatted files consist of only triangle surfaces and the triangle edges are sharp. When dividing STL files to finite elements directly, the triangle surfaces are divided into further small elements resulting in a considerable number of nodes and elements. Therefore, the vertices of the triangle surfaces should be interpolated by mathematically smooth surfaces. This smoothing can be performed using Recap® and Fusion 360® software, both products of Autodesk, Inc. Firstly, the STL files with the triangle meshing were converted to surface models with quad meshing (Figure 4(b)). The quad meshed surfaces were then interpolated and smoothed by T-spline surfaces (Figure 4(c)). Finally, boundary representation solid models were generated based on the T-spline surface models (Figure 4(d)). The resulting solid models were then capable of being analysed in commercial FEA software.

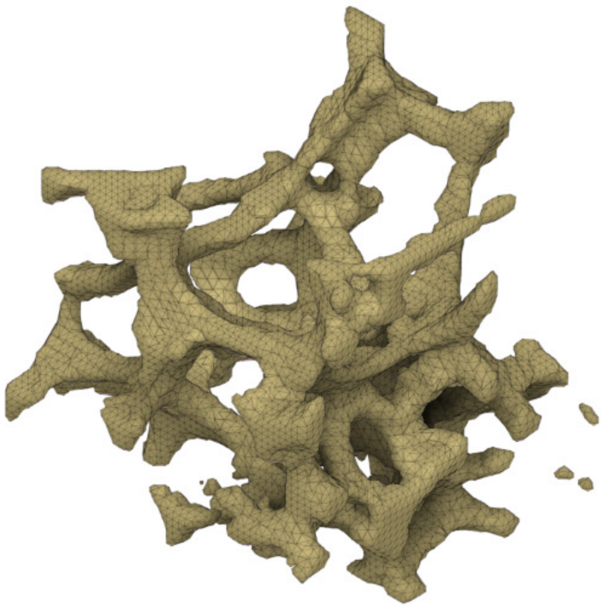

(a)STL file converted from CT scanned images

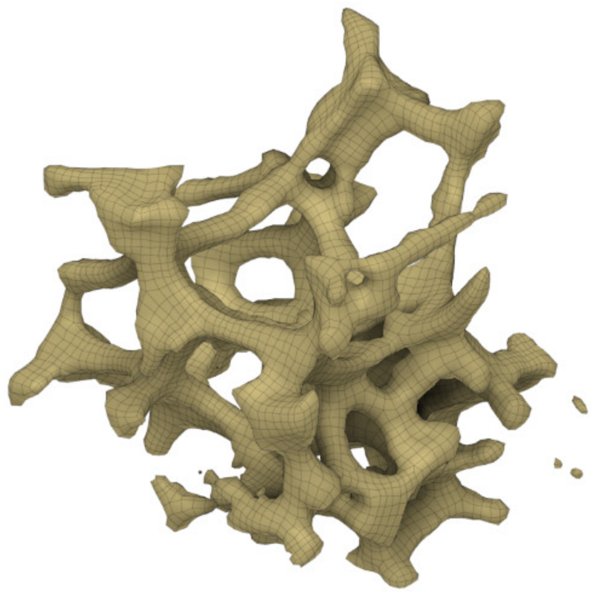

(b)Quad meshed surface model

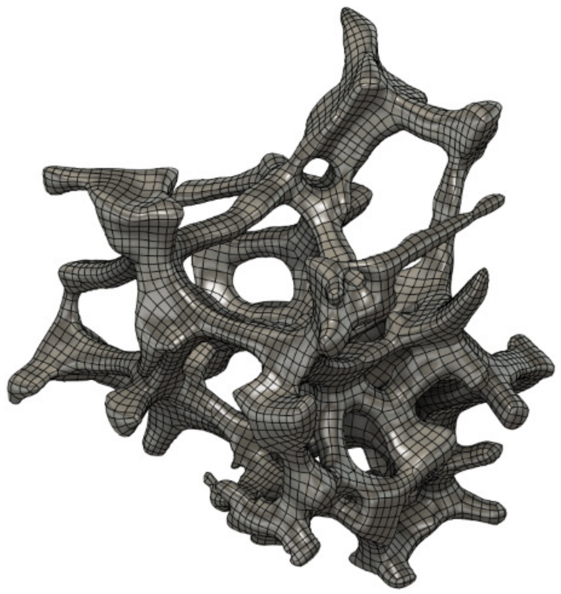

(c)T-spline interpolation

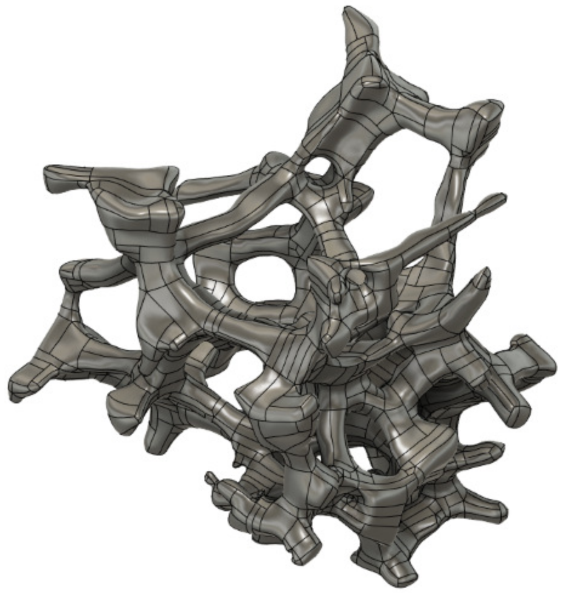

(d)Boundary representation solid model

Figure 4. Conversion from the STL files to the boundary representation solid models

2.5. *Hexahedron dominant meshing*

Although the geometries were smoothed by the T-spline interpolation, they were still too complex for hexahedron meshing to be applied. Therefore, mixed hexahedron and tetrahedron meshing was employed. These two kinds of elements were joined by the pyramid mesh elements. The mesh divisions were performed using Ansys® Academic Research Meshing, Release 19.2 [49]. In this study, three representative geometric models were analysed. The mesh divisions of these models are shown in Figure 5 and Table 1 summarises the numbers of the nodes and the elements in each. Where possible the models were meshed with hexahedron or pyramid elements.

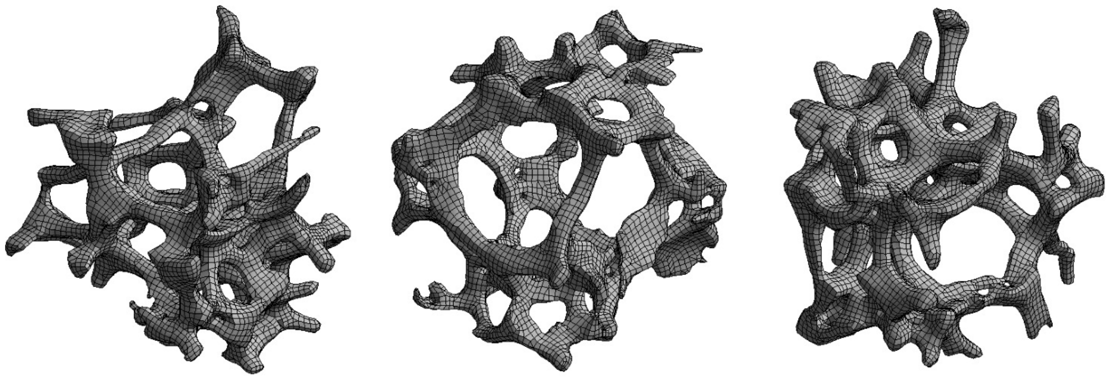

(a)Model A (b)Model B (c)Model C

Figure 5. Mesh divisions for the models

Table 1. Numbers of nodes and elements for the models

	Model A	Model B	Model C
Nodes	27730	24937	30081
Tetrahedron elements	10873	11586	12041
Pyramid elements	16202	16795	17083
Hexahedron elements	13231	13746	15089

2.6. Finite element analyses

Deformation behaviour of 3 different specimen models was calculated with the commercial FEA software Ansys® Academic Research Mechanical, Release 19.2 [50]. To analyse the deformations up to the plateau region, the large deflection was taken into account. As this study focused on the static mechanical properties of polyurethane foams, the static implicit method was employed and the damping or the dynamic characteristics were neglected.

2.7. Strut material model

In order to measure the stress-strain relationship of the matrix material, a specimen without pores is needed. The diameters of the struts are less than 0.1mm and form a complex microstructure. Foam was compressed between plates heated to 150°*C* in order to obtain a parent material specimen without pores. The original thickness of the foam was 50mm and the compressed specimen had a thickness of 0.7mm. The measured density of the specimen was $1200\text{kg}/\text{m}^3$.

Tensile testing was performed to obtain the tensile stress-strain relationship. The test equipment was a universal testing machine AGS-X 10kN with a 500N load cell, products of SHIMADZU CORPORATION. The specimen was cut into $50 \times 5\text{mm}^2$ rectangular shape specimens and then a tensile test was performed under the strain rate 0.01s^{-1}. The difference between the grippers was regarded as the elongation of the specimen.

The measured nominal stress-strain curve is shown in Figure 6. The experimental result is approximated by the Neo-Hookean (Equation (1)) and Mooney Rivlin (Equation (2)) hyper elastic models respectively.

$$W = C_{10}\left(\bar{I}_1 - 3\right) + \frac{1}{d}\left(J - 1\right)^2 \tag{1}$$

$$W = C_{10}\left(\bar{I}_1 - 3\right) + C_{01}\left(\bar{I}_2 - 3\right) + \frac{1}{d}\left(J - 1\right)^2 \tag{2}$$

W is the strain energy density, $\bar{I}_1$ and $\bar{I}_2$ are the first and second deviatoric strain invariants, J is the determinant of the deformation gradient. The material constants C_{10}, C_{01} and d are shown in Table 2. Because the matrix material is thought to be incompressive, d was calculated to let the initial

Poisson's ratio ν equal to 0.48. The Mooney-Rivlin model was employed in this study as it shows better agreement with the experimental result than the Neo-Hookean model.

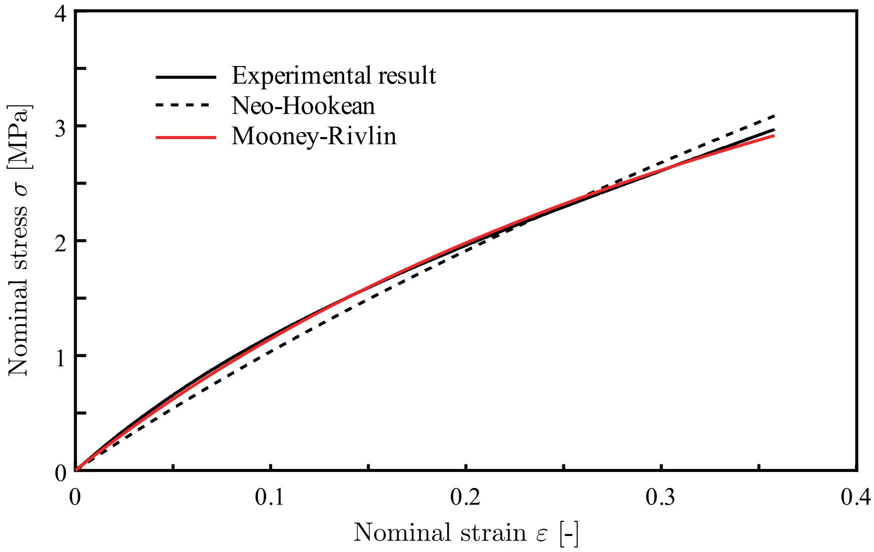

Figure 6. The result of the tensile test for the matrix material and its approximations by hyperelastic models

Table 2. Material constants for the matrix material

Hyperelasticity models	C_{10}[MPa]	C_{01}[MPa]	d[MPa^{-1}]
Neo-Hookean	1.89	-	0.0661
Mooney-Rivlin	0.476	1.78	0.0554

157 *2.8. Boundary conditions*

The foam model specimen was uniaxially compressed between two rigid shell plates Figure 7. The lower plate was fixed preventing any translational or rotational displacements. Translational displacement was applied to the upper plate whilst all other degrees of freedom were constraint. Frictionless contacts between the foam model and the rigid walls were defined using the penalty method with a stiffness factor 0.01. Self-contacts between the struts were not considered as this study focuses on the buckling behaviour in the transitions to the plateau regions. Finally, remote displacements were used to constraint the specimen lateral boundaries from rigid translational and rotational movement. The average values of the displacements of the nodes on the boundaries corresponding to these directions were fixed. This would allow deformation but not rigid body movement.

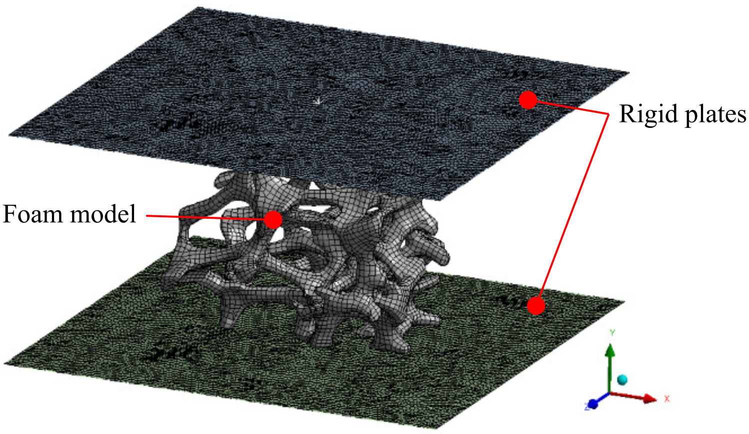

Figure 7. Boundary condition for the uniaxial compression analyses of the foam models

2.9. Experimental measurement for the macroscopic stress strain relationships

The uniaxial compression tests for the actual foam specimens were performed to compare with the FEA results. The testing method was similar to ISO3386-1 [51]. The $25 \times 25 \times 10(\text{mm}^3)$ sized specimens were cut from the centre parts of the moulded foams. The specimens were set into the same equipment as the section 2.7 with the compression plates. The lower plate was perforated by 6mm holes arranged in a latticed pattern with 20mm distances so that the air in the foam could be ventilated. Firstly, the foams were compressed to achieve 75% nominal strain with the speed 50mm/s as the pre-compression. Then, the load was taken off with the same speed and the foams were left for 60s. After that, the foams were compressed again with the same speed and compressive strain to measure the load and the displacement.

3. Results

3.1. The deformed shapes of the models

Figure 8 shows the deformed shapes of the different specimen models at the macroscopic nominal compressive strains $\varepsilon^c = 0.05$, 0.25 and 0.50 respectively. The coloured contour represents the Von-Mises equivalent strains ε^{eq}. As mentioned in the section 1, the struts bend in the linear elastic region ($\varepsilon^c = 0.05$). After that, some struts start to buckle, which indicates a transition to the plateau region ($\varepsilon^c = 0.25$). Finally, the models gradually become denser and transfer into the densification region ($\varepsilon^c = 0.50$). As self-contacts were not applied in the foam models, the struts did not touch, but instead overlapped. The results of the analyses enable the microscopic behaviour of the struts to be carefully observed.

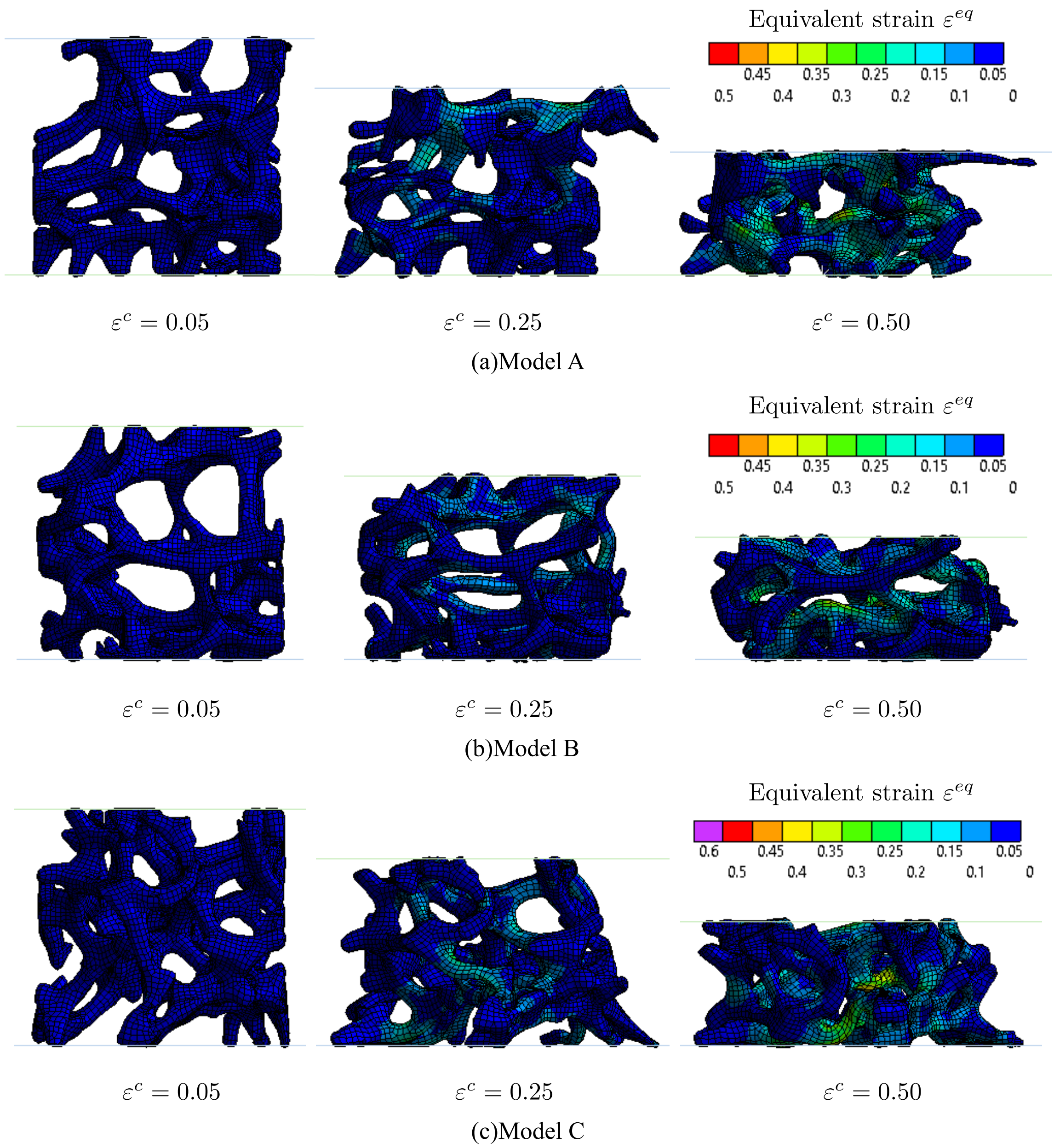

Figure 8. The deformed shapes of the models with the distributions of the equivalent strain ε^{eq}

3.2. Macroscopic stress-strain relationships

The FEA results were compared with the experiment results to validate the accuracy of the presented analysis method. Figure 9 shows the both experimental and FEA results of the relations between the nominal compressive stress and strain. The slopes of the stress-strain curves for the FEA results start decreasing in the strain region around 0.05 compared to the smaller strain region. It is thought to mean the transition from the linear elastic regions to the plateau regions.

The models appear to be in good agreement with experiments in the linear elastic and the plateau regions, and up to the strain of 0.30. Differences of the stresses between the experimental and FEA results at the nominal compressive strain of 0.25 were 0.1%, 16.5% and 6.6% for the models A, B and C respectively. In contrast, the FEA results are stiffer than the experimental results in larger strain regions than 0.30. After reaching the strain of 0.30, the slopes of the stress strain curves start increasing again. This behaviour looks similar to the transition to the densification regions, however, self-contacts were not enabled within the model and the stress increase occurs far too early in the strain regions. The presented method should be modified when applied for the densification region.

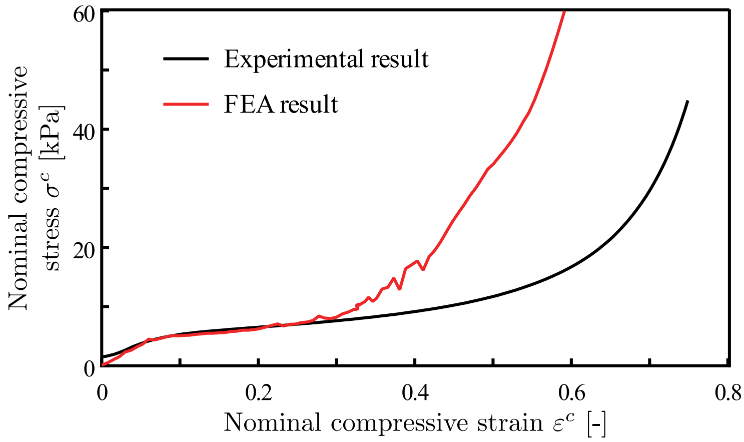

(a)Model A

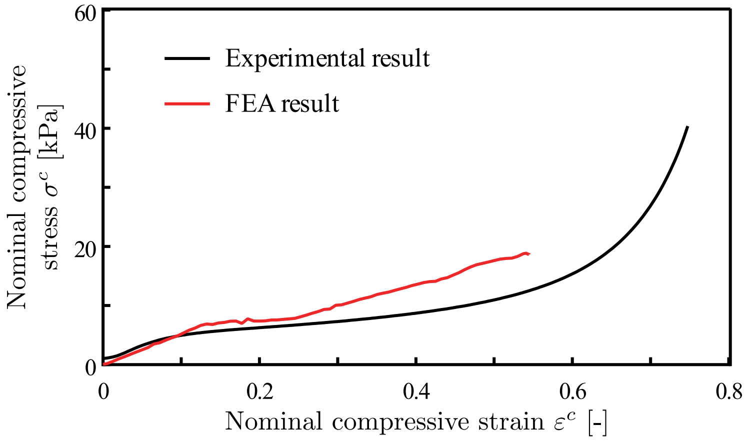

(b)Model B

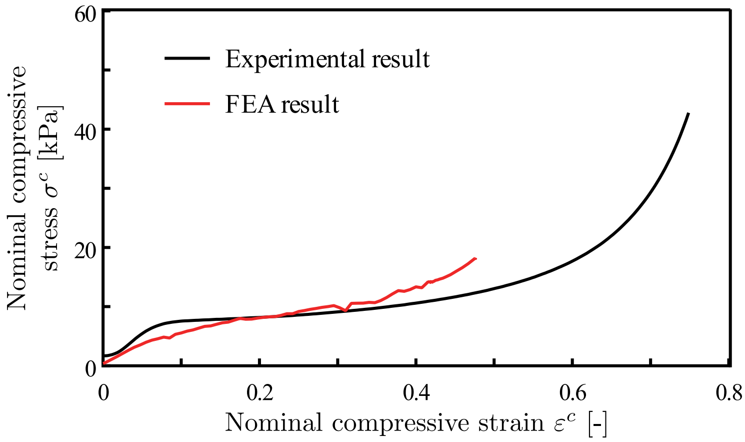

(c)Model C

Figure 9. The experimental and FEA results in the relations between the macroscopic compressive stress and strain

4. Discussions

The compressive response of Polyurethane foam geometries was simulated using FE methods and compared with experiments. Foam specimens were scanned using X-ray CT and analysed to obtain geometries for FE simulations. Simulation results were in good agreement with experiments up to 0.3 strain. The finite element model over-predicted stresses, beyond that strain. Three different specimens were scanned and modelled to ensure repeatability of results.

Elastic buckling appears to be one of the dominant deformation mechanisms. The finite element simulation results seem to have captured the strut deformation behaviour in agreement to relevant literature [1]. Similar deformation mechanisms have been captured with virtually generated cell structures such as Kelvin's cells [2,4,8,9,11,12,23,29] or Voronoi polyhedrons [24,27,30,31]. Previous models based on X-ray CT scanned foam structures were mostly limited to small strains (up to 5.31%) [43–45].

Hexahedron dominant meshing was used for the large deformation analyses. Struts in foam materials can be long and narrow. Euler-Bernoulli beams have been widely employed for analytical calculations [2,4] and numerical simulations [8,9,24,27,29–31]. However whilst beam models might be beneficial in reducing complexity and calculation time, they might also add stiffness to the structure and result in higher stress predictions by comparison to the experiment values. Hexahedron meshes in large deformation problems, have been used for simplified geometries [11,12]. The presented smoothing method and hexahedron dominant meshing are recommended for the complex X-ray scanned geometries.

The foam struts at the lateral specimen boundary were unconstraint. Similarly to other studies [31–33,36,43], compressive loads were applied in the model, by using rigid plates. Contact was defined between the foam specimen and the rigid plates. The modelled specimens were smaller than those used for experiments. However the boundary conditions seem to have been sufficient in capturing the strut behaviour for strains up to 0.3. Due to the high porosity of the foam, the effect of surrounding material at the boundary might have been effectively negligible for up to the strain of interest. However more sophisticated boundary conditions might be required for achieving better accuracy beyond 0.3 strain, or for lower porosity foams. Surrounding cell structures could affect the computed region with bending moments, forces, or contacts between the struts, particularly as the foam densifies. These effects could potentially be taken into account by considering periodic boundary conditions [11,12]. However, this type of boundary condition requires the geometry in the model to be periodic and therefore might be more difficult to apply in models of stochastic foam geometries.

The finite element model over-predicted stresses, beyond 0.3 strain. Figure 10 shows an example of the deformed modelled specimen at 0.3 strain. As the specimen is compressed, struts that were initially away from the boundary, might then deform and come into contact with the loading plates at the boundary of the specimen. This could cause an increase in the stress response. Arguably this could also occur during experiments however the model size is considerably smaller than the specimen size in experiments, therefore the effect of these interactions would be more pronounced in the finite element model simulation. A mitigating approach could be to selectively enable contacts between the loading platens and parts of the foam, i.e. applying contacts only to the nodes on the boundary of the foam rather than the whole specimen. Increasing the model domain size could also improve results. However a larger model would also increase computational cost. A damage model was not included in this study. Potentially the inclusion of a damage model could improve the accuracy at higher stains.

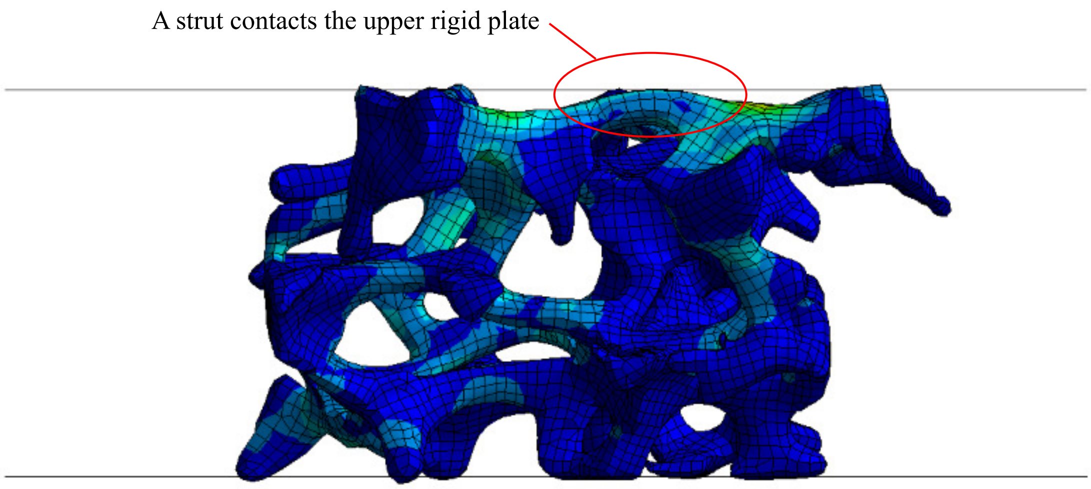

Figure 10. Deformed shape of the model A at the strain of 0.30, when a strut contacts the upper rigid wall

Analysing the models up to the densification region using implicit FE methods, with the periodic boundary conditions or with larger domains remains a challenge. Additionally investigating the effect of strut length and cross-section on the buckling behaviour of struts, and the effect of the cell size variation on the linearity of the stress-strain response could inform manufacturing processes for future products. These would be the topics of future work.

5. Conclusions

Polyurethane foam specimens, intended for automotive seat pads, were scanned using X-ray computed tomography. The scans were converted to 3D CAD models and used to simulate uniaxial compression test using the finite element method. The methodology for the scanning and the analyses was described, and the analysis results were compared with experiments. All three numerical models sufficiently captured the material behaviour in the linear elastic and plateau region of the stress-strain curve. The conclusions for this study are summarised below:

- The investigated foams were scanned by X-ray computed tomography and their structures were captured in 2D cross-section images.
- The observed cross-section images were converted to 3D CAD models using Image J and Autodesk, Inc software products. The smoothed CAD models were analysed with commercial FEA software (Ansys).
- Foam specimens were experimentally tested under uniaxial compression.
- Specimen deformations were analysed by the implicit finite element method with the hexahedron and tetrahedron mixed meshing.
- The mechanical behaviour of foam specimens under compressive loading was sufficiently captured at 0.25 nominal strain and within reasonable error margin.

The presented method was successfully used to analyse foam structures and provided a tool in understanding the mechanism of compressive deformations in polyurethane foams. Commercial CAD products and open source software were used for creating a solid mesh for FE analysis from X-ray scans. The chosen approach was perhaps more efficient by comparison to alternative specialised software at a higher cost or in-house development of custom tools. The dependence of the foam macroscopic mechanical behaviour on microstructural features can now be further investigated to inform manufacturing processes for future polyurethane foam products.

Author Contributions: Conceptualization, M.I.; methodology, M.I. and R.G.; validation, M.I., P.S., B.S. and N.M.; formal analysis, M.I.; investigation, M.I.; writing–original draft preparation, M.I.; writing–review and editing,

M.I., R.G., P.S., B.S. and N.M.; supervision, P.S., B.S. and N.M.; project administration, N.M. All authors have read and agreed to the published version of the manuscript.

Funding: This research received no external funding.

Acknowledgments: The authors kindly acknowledge Bridgestone Corporation, which supplied the specimens for the research.

Conflicts of Interest: The authors declare no conflict of interest.

Abbreviations

The following abbreviations are used in this manuscript:

CT	Computed tomography
FEA	Finite element analysis
PUF	Polyurethane foam

References

1. Gibson, L.J.; Ashby, M.F., The mechanics of foams: basic results. In *Cellular Solids: Structure and Properties*, 2 ed.; Cambridge Solid State Science Series, Cambridge University Press, 1997; pp. 175–234. doi:10.1017/CBO9781139878326.007.
2. Zhu, H.X.; Knott, J.F.; Mills, N.J. Analysis of the elastic properties of open-cell foams with tetrakaidecahedral cells. *Journal of the Mechanics and Physics of Solids* **1997**, *45*, 319–343. doi:10.1016/S0022-5096(96)00090-7.
3. Zhu, H.X.; Mills, N.J.; Knott, J.F. Analysis of the high strain compression of open-cell foams. *Journal of the Mechanics and Physics of Solids* **1997**, *45*, 1875–1899. doi:10.1016/S0022-5096(97)00027-6.
4. Mills, N.J.; Zhu, H.X. The high strain compression of closed-cell polymer foams. *Journal of the Mechanics and Physics of Solids* **1999**, *47*, 669–695. doi:10.1016/S0022-5096(98)00007-6.
5. Zhu, H.X.; Mills, N.J. Modelling the creep of open-cell polymer foams. *Journal of the Mechanics and Physics of Solids* **1999**, *47*, 1437–1457. doi:10.1016/S0022-5096(98)00116-1.
6. Laroussi, M.; Sab, K.; Alaoui, A. Foam mechanics: Nonlinear response of an elastic 3D-periodic microstructure. *International Journal of Solids and Structures* **2002**, *39*, 3599–3623. doi:10.1016/S0020-7683(02)00172-5.
7. Gong, L.; Kyriakides, S.; Jang, W.Y. Compressive response of open-cell foams. Part I: Morphology and elastic properties. *International Journal of Solids and Structures* **2005**, *42*, 1355–1379. doi:10.1016/j.ijsolstr.2004.07.023.
8. Gong, L.; Kyriakides, S. Compressive response of open cell foams part II: Initiation and evolution of crushing. *International Journal of Solids and Structures* **2005**, *42*, 1381–1399. doi:10.1016/j.ijsolstr.2004.07.024.
9. Gong, L.; Kyriakides, S.; Triantafyllidis, N. On the stability of Kelvin cell foams under compressive loads. *Journal of the Mechanics and Physics of Solids* **2005**, *53*, 771–794.
10. Demiray, S.; Becker, W.; Hohe, J. Numerical determination of initial and subsequent yield surfaces of open-celled model foams. *International Journal of Solids and Structures* **2007**, *44*, 2093–2108. doi:10.1016/j.ijsolstr.2006.06.044.
11. Okumura, D.; Okada, A.; Ohno, N. Buckling behavior of Kelvin open-cell foams under [0 0 1], [0 1 1] and [1 1 1] compressive loads. *International Journal of Solids and Structures* **2008**, *45*, 3807–3820. doi:10.1016/j.ijsolstr.2007.10.021.
12. Takahashi, Y.; Okumura, D.; Ohno, N. Yield and buckling behavior of Kelvin open-cell foams subjected to uniaxial compression. *International Journal of Mechanical Sciences* **2010**, *52*, 377–385. doi:10.1016/j.ijmecsci.2009.10.009.
13. Ye, W.; Barbier, C.; Zhu, W.; Combescure, A.; Baillis, D. Macroscopic multiaxial yield and failure surfaces for light closed-cell foams. *International Journal of Solids and Structures* **2015**, *69-70*, 60–70. doi:10.1016/j.ijsolstr.2015.06.008.
14. Zhu, H.X.; Hobdell, J.R.; Windle, A.H. Effects of cell irregularity on the elastic properties of open-cell foams. *Acta Materialia* **2000**, *48*, 4893–4900.

15. Zhu, H.X.; Hobdell, J.R.; Windle, A.H. EEects of cell irregularity on the elastic properties of 2D Voronoi honeycombs. *Journal of the Mechanics and Physics of Solids* **2001**, *49*, 857–870.
16. Zhu, H.X.; Windle, A.H. Effects of cell irregularity on the high strain compression of open-cell foams. *Acta Materialia* **2002**, *50*, 1041–1052.
17. Zhu, W.; Blal, N.; Cunsolo, S.; Baillis, D. Micromechanical modeling of effective elastic properties of open-cell foam. *International Journal of Solids and Structures* **2017**, *115-116*, 61–72. doi:10.1016/j.ijsolstr.2017.02.031.
18. Marvi-Mashhadi, M.; Lopes, C.S.; LLorca, J. Effect of anisotropy on the mechanical properties of polyurethane foams: An experimental and numerical study. *Mechanics of Materials* **2018**, *124*, 143–154. doi:10.1016/j.mechmat.2018.06.006.
19. Marvi-Mashhadi, M.; Lopes, C.S.; LLorca, J. Surrogate models of the influence of the microstructure on the mechanical properties of closed- and open-cell foams. *Journal of Materials Science* **2018**, *53*, 12937–12948. doi:10.1007/s10853-018-2598-4.
20. Jang, W.Y.; Kraynik, A.M.; Kyriakides, S. On the microstructure of open-cell foams and its effect on elastic properties. *International Journal of Solids and Structures* **2008**, *45*, 1845–1875. doi:10.1016/j.ijsolstr.2007.10.008.
21. Storm, J.; Abendroth, M.; Emmel, M.; Liedke, T.; Ballaschk, U.; Voigt, C.; Sieber, T.; Kuna, M. Geometrical modelling of foam structures using implicit functions. *International Journal of Solids and Structures* **2013**, *50*, 548–555. doi:10.1016/j.ijsolstr.2012.10.026.
22. Storm, J.; Abendroth, M.; Zhang, D.; Kuna, M. Geometry dependent effective elastic properties of open-cell foams based on kelvin cell models. *Advanced Engineering Materials* **2013**, *15*, 1292–1298. doi:10.1002/adem.201300141.
23. Zhang, D.; Abendroth, M.; Kuna, M.; Storm, J. Multi-axial brittle failure criterion using Weibull stress for open Kelvin cell foams. *International Journal of Solids and Structures* **2015**, *75-76*, 1–11. doi:10.1016/j.ijsolstr.2015.04.020.
24. Storm, J.; Abendroth, M.; Kuna, M. Numerical and analytical solutions for anisotropic yield surfaces of the open-cell Kelvin foam. *International Journal of Mechanical Sciences* **2016**, *105*, 70–82. doi:10.1016/j.ijmecsci.2015.10.014.
25. Zhu, W.; Blal, N.; Cunsolo, S.; Baillis, D. Effective elastic properties of periodic irregular open-cell foams. *International Journal of Solids and Structures* **2018**, *143*, 155–166. doi:10.1016/j.ijsolstr.2018.03.003.
26. Zhu, W.; Blal, N.; Cunsolo, S.; Baillis, D.; Michaud, P.M. Effective elastic behavior of irregular closed-cell foams. *Materials* **2018**, *11*. doi:10.3390/ma11112100.
27. Storm, J.; Abendroth, M.; Kuna, M. Effect of morphology, topology and anisoptropy of open cell foams on their yield surface. *Mechanics of Materials* **2019**, *137*, 103145. doi:10.1016/j.mechmat.2019.103145.
28. Jang, W.Y.; Kyriakides, S. On the crushing of aluminum open-cell foams: Part I. Experiments. *International Journal of Solids and Structures* **2009**, *46*, 617–634. doi:https://doi.org/10.1016/j.ijsolstr.2008.09.008.
29. Jang, W.Y.; Kyriakides, S. On the crushing of aluminum open-cell foams: Part II analysis. *International Journal of Solids and Structures* **2009**, *46*, 635–650. doi:10.1016/j.ijsolstr.2008.10.016.
30. Jang, W.Y.; Kyriakides, S.; Kraynik, A.M. On the compressive strength of open-cell metal foams with Kelvin and random cell structures. *International Journal of Solids and Structures* **2010**, *47*, 2872–2883. doi:10.1016/j.ijsolstr.2010.06.014.
31. Gaitanaros, S.; Kyriakides, S.; Kraynik, A.M. On the crushing response of random open-cell foams. International Journal of Solids and Structures, 2012, Vol. 49, pp. 2733–2743. doi:10.1016/j.ijsolstr.2012.03.003.
32. Gaitanaros, S.; Kyriakides, S. On the effect of relative density on the crushing and energy absorption of open-cell foams under impact. *International Journal of Impact Engineering* **2015**, *82*, 3–13. doi:10.1016/j.ijimpeng.2015.03.011.
33. Gaitanaros, S.; Kyriakides, S.; Kraynik, A.M. On the crushing of polydisperse foams. *European Journal of Mechanics, A/Solids* **2018**, *67*, 243–253. doi:10.1016/j.euromechsol.2017.09.010.
34. Storm, J.; Abendroth, M.; Kuna, M. Influence of curved struts, anisotropic pores and strut cavities on the effective elastic properties of open-cell foams. *Mechanics of Materials* **2015**, *86*, 1–10. doi:10.1016/j.mechmat.2015.02.012.

35. Barnes, A.T.; Ravi-Chandar, K.; Kyriakides, S.; Gaitanaros, S. Dynamic crushing of aluminum foams: Part I - Experiments. *International Journal of Solids and Structures* **2014**, *51*, 1631–1645. doi:10.1016/j.ijsolstr.2013.11.019.
36. Gaitanaros, S.; Kyriakides, S. Dynamic crushing of aluminum foams: Part II - Analysis. *International Journal of Solids and Structures* **2014**, *51*, 1646–1661. doi:10.1016/j.ijsolstr.2013.11.020.
37. Yang, C.; Kyriakides, S. Multiaxial crushing of open-cell foams. *International Journal of Solids and Structures* **2019**, *159*, 239–256. doi:10.1016/j.ijsolstr.2018.10.005.
38. Jones, A.C.; Arns, C.H.; Sheppard, A.P.; Hutmacher, D.W.; Milthorpe, B.K.; Knackstedt, M.A. Assessment of bone ingrowth into porous biomaterials using MICRO-CT. *Biomaterials* **2007**, *28*, 2491–2504. doi:https://doi.org/10.1016/j.biomaterials.2007.01.046.
39. John, Ł.; Janeta, M.; Rajczakowska, M.; Ejfler, J.; Łydżba, D.; Szafert, S. Synthesis and microstructural properties of the scaffold based on a 3-(trimethoxysilyl)propyl methacrylate–POSS hybrid towards potential tissue engineering applications. *RSC Adv.* **2016**, *6*, 66037–66047. doi:10.1039/C6RA10364B.
40. Munkholm, L.J.; Heck, R.J.; Deen, B. Soil pore characteristics assessed from X-ray micro-CT derived images and correlations to soil friability. *Geoderma* **2012**, *181-182*, 22–29. doi:https://doi.org/10.1016/j.geoderma.2012.02.024.
41. Patterson, B.M.; Henderson, K.; Gilbertson, R.D.; Tornga, S.; Cordes, N.L.; Chavez, M.E.; Smith, Z. Morphological and Performance Measures of Polyurethane Foams Using X-Ray CT and Mechanical Testing. *Microscopy and Microanalysis* **2014**, *20*, 1284–1293. doi:10.1017/S1431927614000993.
42. Ulrich, D.; van Rietbergen, B.; Weinans, H.; Rüegsegger, P. Finite element analysis of trabecular bone structure: a comparison of image-based meshing techniques. *Journal of Biomechanics* **1998**, *31*, 1187–1192. doi:https://doi.org/10.1016/S0021-9290(98)00118-3.
43. Jeon, I.; Asahina, T.; Kang, K.J.; Im, S.; Lu, T.J. Finite element simulation of the plastic collapse of closed-cell aluminum foams with X-ray computed tomography. *Mechanics of Materials* **2010**, *42*, 227–236. doi:https://doi.org/10.1016/j.mechmat.2010.01.003.
44. Zhang, L.; Ferreira, J.M.F.; Olhero, S.; Courtois, L.; Zhang, T.; Maire, E.; Rauhe, J.C. Modeling the mechanical properties of optimally processed cordierite–mullite–alumina ceramic foams by X-ray computed tomography and finite element analysis. *Acta Materialia* **2012**, *60*, 4235–4246. doi:https://doi.org/10.1016/j.actamat.2012.04.025.
45. Natesaiyer, K.; Chan, C.; Sinha-Ray, S.; Song, D.; Lin, C.L.; Miller, J.D.; Garboczi, E.J.; Forster, A.M. X-ray CT imaging and finite element computations of the elastic properties of a rigid organic foam compared to experimental measurements: insights into foam variability. *Journal of Materials Science* **2015**, *50*, 4012–4024. doi:10.1007/s10853-015-8958-4.
46. Schindelin, J.; Arganda-Carreras, I.; Frise, E.; Kaynig, V.; Longair, M.; Pietzsch, T.; Preibisch, S.; Rueden, C.; Saalfeld, S.; Schmid, B.; Tinevez, J.Y.; White, D.J.; Hartenstein, V.; Eliceiri, K.; Tomancak, P.; Cardona, A. Fiji: an open-source platform for biological-image analysis. *Nature Methods* **2012**, *9*, 676–682. doi:10.1038/nmeth.2019.
47. Rueden, C.T.; Schindelin, J.; Hiner, M.C.; DeZonia, B.E.; Walter, A.E.; Arena, E.T.; Eliceiri, K.W. ImageJ2: ImageJ for the next generation of scientific image data. *BMC Bioinformatics* **2017**, *18*, 529. doi:10.1186/s12859-017-1934-z.
48. Otsu, N. A Threshold Selection Method from Gray-Level Histograms. *IEEE Transactions on Systems, Man, and Cybernetics* **1979**, *9*, 62–66. doi:10.1109/TSMC.1979.4310076.
49. *Ansys® Academic Research Meshing, Release 19.2, Help System, Meshing User's Guide*; ANSYS, Inc.
50. *Ansys® Academic Research Mechanical, Release 19.2, Help System, Mechanical User's Guide*; ANSYS, Inc.
51. *Polymeric materials, cellular flexible — Determination of stress-strain characteristics in compression — Part 1: Low-density materials (ISO Standard No. 3386-1:1986)*; International Organization for Standardization, 1986.